INTERNATIONAL JOURNAL OF CLIMATOLOGY
Int. J. Climatol. (2015)
Published online in Wiley Online Library
(wileyonlinelibrary.com) DOI: 10.1002/joc.4430

RMetS
Royal Meteorological Society

Summer heat waves in southeastern Patagonia: an analysis of the intraseasonal timescale

Martín Jacques-Coper,[a]* Stefan Brönnimann,[a] Olivia Martius,[a] Carolina Vera[b] and Bibiana Cerne[b]

[a] *Oeschger Centre for Climate Change Research and Institute of Geography, University of Bern, Switzerland*
[b] *CIMA/CONICET-UBA, DCAO/FCEN, UMI-IFAECI/CNRS, Universidad de Buenos Aires, Argentina*

ABSTRACT: We explore the occurrence of intraseasonal summer heat waves in southeastern Patagonia (SEPG, 46°–52°S; 65°–70°W) since the late 19th century by means of the Twentieth Century Reanalysis version 2 (20CRv2). In total, we identify 201 cases for 1872–2010 using criteria of intensity and persistence. In SEPG, the corresponding intraseasonal temperature signals are centred around the first day of each cluster of days fulfilling those conditions (named day 0). The mean warm deviation lasts for approximately 2 weeks and exhibits a mean temperature peak of 4.3 °C on day 0 (the warmest day in the mean signal). In a regional context, the mean temperature perturbation associated with these heat waves affects a broad area on both sides of the Andes. The warming in SEPG is caused by temperature advection and enhanced radiative heating, following a high pressure system over southern South America (SSA). This atmospheric perturbation is embedded in a wave-train-like pattern along the South Pacific. As part of this pattern, a cyclonic anomaly progresses eastward over the Tasman Sea in Oceania, moving from southeastern Australia (day −6, causing a dry anomaly there) over New Zealand (day −3, inducing a wet anomaly on its Southern Island). The anomalous circulation triggered by the wave train leads thus to a teleconnection between SSA and Oceania, documented in a previous work for the interannual scale. Two thirds of the heat wave events are linked to enhanced ascent in the South Atlantic Convergence Zone (SACZ) and around one third of the events within 1957–2010 are associated with extreme absolute maximum temperatures observed at a station-based record from SEPG. Finally, possible spatial modulations of the wave train pattern at the interannual and interdecadal timescales are discussed.

KEY WORDS intraseasonal variability; heat waves; temperature; warm season; South America; Patagonia; Oceania

Received 24 November 2014; Revised 12 May 2015; Accepted 2 June 2015

1. Introduction

Southern South America (SSA, see Table 1 for a list of acronyms) is defined in this work as the part of the continent to the south of 30°S. Patagonia, within SSA, is the region that spans from 40°S until the southern tip of the continent. Although the current climate of Patagonia has been reviewed in a regional and comprehensive context, including its links with the large-scale circulation (e.g. Prohaska, 1976; Paruelo *et al.*, 1998; Garreaud *et al.*, 2012), and also with focus on particular aspects of single variables such as temperature (e.g. Garreaud, 2000; Berman *et al.*, 2013) and precipitation (e.g. Carrasco *et al.*, 2002; Berman *et al.*, 2012), it still remains a relatively unexplored topic in the climate sciences. The relative lack of studies about this region is due in part to the low density of instrumental coverage, especially in the interior regions (Paruelo *et al.*, 1998). Nevertheless, detailed analysis on a broad variety of meteorological and climatological phenomena in Patagonia are needed in order to understand their impacts on natural aspects, such as the biosphere (Lara *et al.*, 2005; Hertel *et al.*, 2008) and cryosphere (Carrasco *et al.*, 2002; Rignot *et al.*, 2003; Rasmussen *et al.*, 2007), but also on socioecological subjects, such as desertification (Del Valle *et al.*, 1998; Mazzonia and Vazquez, 2009). In particular, a valuable motivation to perform further research within these various fields is to get a better knowledge on transient subseasonal warm episodes in Patagonia, which is the main topic addressed in this paper.

On the western side of Patagonia, the interaction between the westerly flow from the Pacific Ocean and the southern Andes leads to a temperate and hyperhumid climate. The eastern side of Patagonia exhibits a continental climate with high aridity caused by the rain shadow effect of the Andes, along with a high annual thermal amplitude and extremely windy conditions associated with the westerlies (Garreaud *et al.*, 2012). Our region of study is southeastern Patagonia (SEPG), defined as the region confined within 46°–52°S; 65°–70°W (Figure 1(a)), which roughly corresponds to the Argentinean province of Santa Cruz. The northeast coast of SEPG exhibits a mild semiarid climate, with mean daily maximum (minimum) temperatures ranging between 24 and 26 °C (12 and 14 °C) during austral summer (December to February, DJF) and scarce annual precipitation (∼230 mm). Further to the south, the conditions correspond rather

* Correspondence to: M. Jacques-Coper, Oeschger Centre for Climate Change Research and Institute of Geography, University of Bern, Hallerstrasse 12, Bern CH-3012, Switzerland. E-mail: jacques@giub.unibe.ch

Table 1. Acronyms used in this paper.

Acronym	Meaning
20CRv2	Twentieth Century Reanalysis version 2
ENSO	El Niño-Southern Oscillation
MJO	Madden–Julian Oscillation
PDO	Pacific Decadal Oscillation
PSA mode	Pacific-South American mode
Prate	Precipitation rate
R1, R2, R3, R4	Regions 1–4
SACZ	South Atlantic Convergence Zone
A_SACZ/NA_SACZ	Active SACZ/non-active SACZ
SAM	Southern Annular Mode
SAT, T	Surface air temperature
SEPG	Southeastern Patagonia (same as Region 3)
SLP	Sea level pressure
SSA	Southern South America (south of 30°S)
T_n, T_x, T_m	Instrumental minimum, maximum, and mean temperature

to a cooler and wetter steppe climate, with maximum (minimum) temperatures fluctuating between 19 and 21 °C (7 and 8 °C).

The modulation of surface air temperature (SAT) in SSA involves various time scales and possible interactions between them. The interdecadal and interannual modulation of summer SAT there was extensively studied by Jacques-Coper and Brönnimann (2014). The summer interannual variability leads to strong regional SAT departures from the climatology in SSA. The leading interannual variability mode, whose strongest spectral peak appears at ∼3.4 years, is related to a wave train pattern in geopotential height at 500 hPa over the South Pacific, which resembles the Pacific-South American (PSA) mode 2. The circulation induced by the centres of action of this pattern causes an interannual teleconnection (anticorrelation) between temperature in SSA and precipitation in Southeastern Australia. The development of this wave-train-like pattern and its climate impacts within the intraseasonal frequency band deserve attention and is a further motivation for this work.

As an analogy to the occurrence of warm summers in SSA in the interannual timescale, in this paper we investigate the intraseasonal modulation of SAT in SEPG by studying the occurrence of local heat waves. Cerne and Vera (2011) analysed summertime intraseasonal heat waves recorded by a single station in Central-Eastern Argentina (Rosario Aero, 32.92°S; 60.78°W) during 1979–2003 using the NCEP–NCAR Reanalysis (Kalnay *et al.*, 1996). For that region, they ascribed 32% of SAT variance to intraseasonal variability. That study also found that 73% of the heat waves detected in Rosario were related to enhanced convection in the South Atlantic Convergence Zone (SACZ, Figure 1(a)), located to the northeast of Rosario. Therefore, it is also of our concern to investigate whether heat waves in diverse regions of SSA are related to each other, and also whether there is a connection between heat wave events detected in SEPG and the SACZ activity.

Cerne and Vera (2011) also identified a large-scale Rossby wave train pattern in association with the heat waves in subtropical South America, which they linked to convection anomalies at the equatorial western and central Pacific Ocean. This pattern, although comparable to the one described for the interannual timescale in SSA by Jacques-Coper and Brönnimann (2014), shows a different phasing of its action centres. Moreover, Rossby wave trains between Oceania and South America have been identified in connection to various climatological phenomena, such as the synoptic incursion of cold air in subtropical South America (Garreaud, 2000), generalized frosts in central–southern South America (Müller and Berri, 2007), cold surge episodes over southeastern Brazil (Sprenger *et al.*, 2013), and the intraseasonal variability of precipitation in subtropical and extratropical South America (e.g. Gonzalez and Vera, 2014). The development of atmospheric Rossby wave trains has been widely described in the literature (e.g. Hoskins *et al.*, 1977) and they can be, indeed, partly induced by tropical forcing (Berbery and Nogués-Paegle, 1993; Jin and Hoskins, 1995). Hence, a another main motivation for this study is to investigate whether warm intraseasonal anomalies in SEPG are also related to a large-scale wave-train-like circulation pattern over the South Pacific.

Robertson and Mechoso (2003) found that the subseasonal circulation in the South Pacific region exhibits three to four recurrent geographically fixed regimes, which are a linear combination of PSA 1 and 2, for all seasons but summer. These patterns are restricted to the mid-latitudes and do not extend into the tropics, in contrast to the findings by Mo and Higgins (1998). Robertson and Mechoso (2003) also documented an oscillation of 42.5 days dominated by the PSA 1 pattern, more pronounced in austral winter and spring, which shows a rapid attenuation and an eastward drift. In summary, they proposed an oscillation of circulation anomalies in the South Pacific that is predominantly stationary in space, but with regimes that account for the slow part of that oscillation. Relatively less work has focused on the way these circulation patterns spread throughout a broad frequency range. Cazes-Boezio *et al.* (2003) found an extratropical teleconnection between ENSO and southeastern South America for austral spring due to a wave train pattern over the South Pacific, which disappears during summer and appears in autumn again (but not related to ENSO). Three wave-train-like circulation regimes were found for intraseasonal 700-hPa geopotential height fields in all seasons. Interannual 200-hPa circulation patterns were found to be related to the frequency of occurrence of those intraseasonal regimes for spring and autumn only. Therefore, we speculate that the connection between different timescales during summer may not be due to the frequency of occurrence of intraseasonal circulation patterns but that strong and/or persistent intraseasonal anomalies would imprint their signal in the seasonal means, thus contributing significantly to the construction of the interannual variability. Therefore, we also aim to study the link between both timescales.

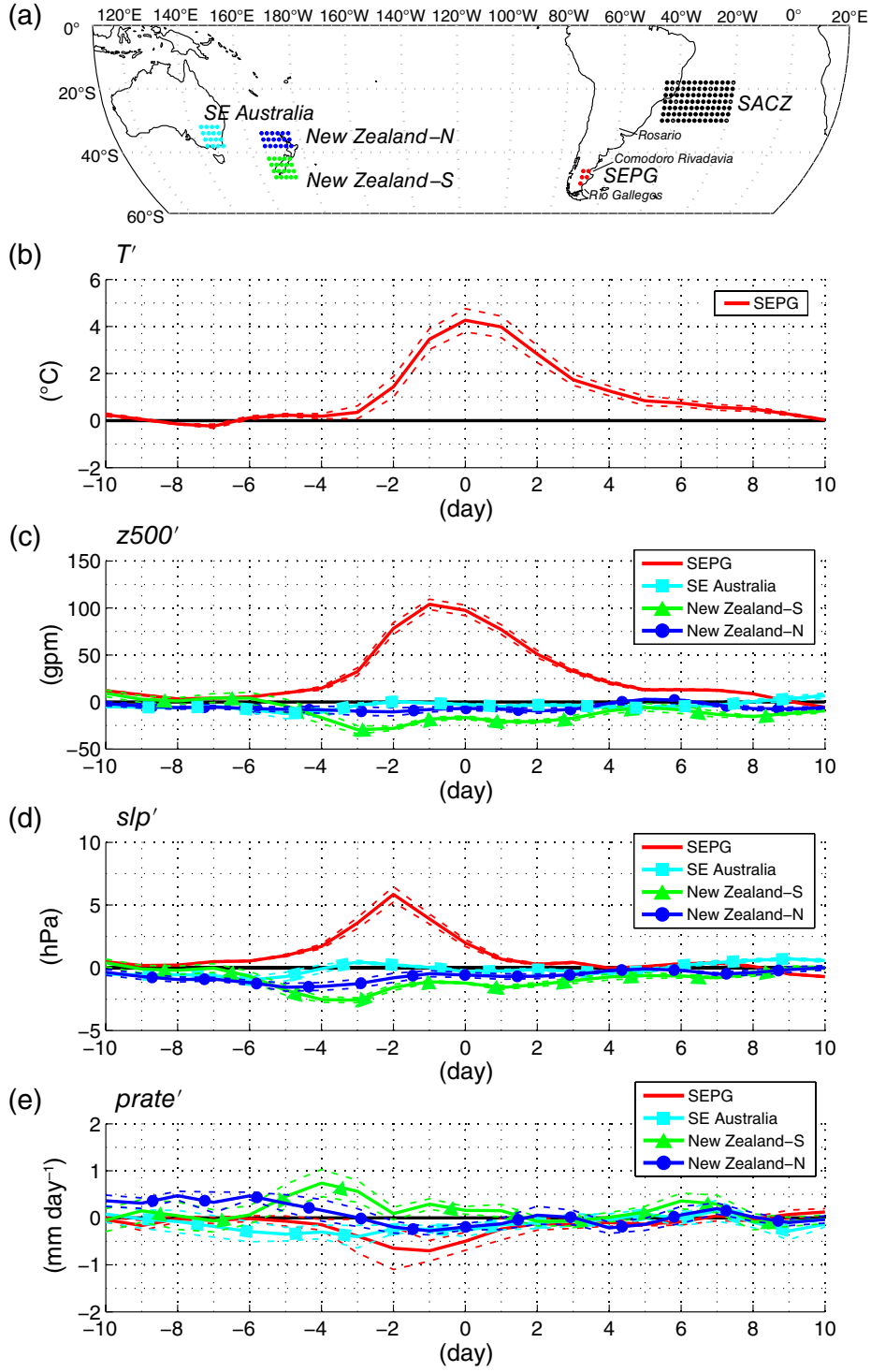

Figure 1. (a) Regions analysed in this study: SEPG (red, 46°–52°S; 65°–70°W), SACZ (black, 18°–30°S; 20°–44°W), SE Australia (cyan, 30°–39°S; 144°–150°E), North Island of New Zealand (blue, 32°–38°S; 166°–178°E), South Island of New Zealand (green 42°–50°S; 166°–176°E). (b–e) 21-day mean time series of T', z500′, slp′ and prate′, respectively, centred on day 0, calculated from the 201 heat waves in SEPG. Continuous (dashed) curves correspond to the composite spatial mean (1 composite spatial standard deviation) of the time series from the gridpoints located within the corresponding regions.

To explore the research topics listed above, in this paper we address the development of heat waves in the intraseasonal timescale over SEPG during 1872–2010. We explore the regional and large-scale aspects associated with our research subject, reproduced by the Twentieth Century Reanalysis version 2 (20CRv2, Compo *et al.*, 2011). In addition, century-long daily climatic records are used to compare and partially validate the results obtained. The data and methods used are described in Section 2. In Section 3, we describe the identification of heat waves in SEPG and discuss their regional manifestation. Besides, we interpret the large-scale circulation

anomalies associated with these events, with a focus on Oceania, in order to understand, in the intraseasonal band, the covariability between SAT in SSA and precipitation in SE Australia and New Zealand. In Section 4, we explore the link between the heat waves in SEPG and the activity of the SACZ. Section 5 presents the analysis on the potential connection between the intraseasonal and interannual patterns that lead to SAT perturbations in SSA, and on a possible decadal variation of the waveguide of these intraseasonal circulation anomalies. Finally, Section 6 summarizes our findings and conclusions.

2. Data and methods

We use non-detrended daily fields of SAT (2 m), mean pressure at sea level (SLP), geopotential height at 500 hPa (z500), precipitation rate (prate), and vertical velocity at 500 hPa (ω500) from the ensemble mean of 20CRv2. Vertical velocity at 500 hPa was selected to investigate large-scale ascent and descent. We focus on DJF (1 December to 28 February) during 1872–2010 (DJF seasons are assigned to the corresponding JF year). Data sets from reanalyses, especially before the satellite era that started around 1979, are based on observations that are spatially scarce, in particular in the Southern Hemisphere. This fact may reduce the reliability of these products in early decades of the study period; however, the summer season was found to exhibit better skill in some data sets (Bromwich *et al.*, 2007). The 20CRv2 comprises a state-of-the-art assimilation mechanism of observations taken at the surface (SLP and sea surface temperature) that allows a reliable spatiotemporal reconstruction of the atmosphere (Compo *et al.*, 2011). For instance, during 1958–1978, the skill of this product compared with radiosonde observations at 300 hPa in the Southern Hemisphere extratropics overtakes that of the ERA40 reanalysis (Uppala *et al.*, 2005; Compo *et al.*, 2011). Partly because of its novelty, the 20CRv2 has not been extensively used for studies focusing on the Southern Hemisphere. However, previous works have assessed this data set positively, and stressed its quality and usefulness (Brönnimann *et al.*, 2011, 2012; Zhang *et al.*, 2012; Wang and Cai, 2013; Jacques-Coper and Brönnimann, 2014). In this study, we explicitly consider instrumental measurements in order to compare and corroborate the results extracted from 20CRv2.

The intraseasonal anomalies are defined following the method of Cerne and Vera (2011) as the result of subtracting from the daily values the climatological daily mean (annual cycle) and the seasonal departures of every year from the climatology (i.e. the DJF mean of each year minus the long-term seasonal mean). In other words, we consider that the absolute temperature for a certain day is made of the sum of the expected long-term value defined by the yearly cycle plus the mean seasonal anomaly of the corresponding year plus the intraseasonal anomaly, which accounts for the higher frequency perturbation. That is, the intraseasonal anomaly of a given variable for a certain day d and year y is calculated as follows:

$$\begin{aligned}&\text{Intraseasonal anomaly}_{d,y}\\&= \text{daily value}_{d,y} - \text{climatological daily mean}_{d}\\&\quad - \left(\text{DJF seasonal mean}_{y} - \text{long-term DJF seasonal mean}\right)\end{aligned} \tag{1}$$

The reference period for defining long-term statistics (mean, standard deviation, seasonal cycle, etc.) and anomalies is 1961–1990. For simplicity, in the rest of the paper, a prime will denote intraseasonal variables.

We first calculate daily SAT anomalies on the intraseasonal timescale (T') as the spatial mean of the five gridpoints within SEPG (Figure 1(a)). Then, we detect heat waves using the following criteria (Cerne and Vera, 2011), which must be met at the same time: (1) $T' > 0$ for at least five consecutive days, and (2) T' larger than its own standard deviation for at least three consecutive days. The definition of *intraseasonal anomalies* used in this study has the advantage of filtering out the variability portion related to lower frequencies. Thus, in order to identify the heat waves, we subtract from the temperature signal the background set up, for instance, by a relatively cold or warm summer in the study region and focus on relative temperature perturbations with respect to that background. In this way, we do not explore *absolute* heat waves regarding the actual measured temperature. Hence, a larger number of cases can be analysed and a deeper insight into the intraseasonal frequency band is gained. A similar analysis is performed considering the other variables included in this paper.

Near-surface temperature advection was calculated at 925 hPa for the zonal and meridional components on a daily basis, through the centred finite difference method, using 20CRv2 fields. Horizontal temperature advection results as the sum of both components.

For the comparison between different timescales, mean seasonal (i.e. *interannual*, summer-to-summer) DJF SAT anomalies were calculated for SEPG, based on the series obtained following this methodology: (1) detrending of the *raw* DJF seasonal mean series, using the least-squares fit of a straight line, (2) computation of the interdecadal component of the series calculated in *step 1*, by applying to it a 7-years running mean twice (which consequently reduced its length at the beginning and the end by 6 years each), and (3) subtraction of the series obtained in *step 2* from that obtained in *step 1*. Warm (cold) summers were defined as those seasons above (below) one interannual (summer-to-summer) standard deviation (0.63 °C), considering 1878–2004.

Temperature observations (minimum temperature, T_n, maximum temperature, T_x, and mean temperature, T_m, calculated as the average of T_n and T_x) from the stations Comodoro Rivadavia Aero (45.78°S; 67.50°W, 46 m a.s.l.) and Río Gallegos Aero (51.62°S; 69.28°W, 19 m a.s.l.; their locations are shown in Figures 1 and 3) span 1957–2010 and were supplied by the Argentinean National Weather Service. Their intraseasonal anomalies were obtained in a similar way as those from

the reanalysis data. Precipitation records from Oceania were provided by the Australian Bureau of Meteorology (Cataract Dam Station, Southeastern Australia: 34.26°S; 150.81°E, 340 m a.s.l., used record length: NDJFM 1905–2006) and the New Zealand National Climate Database (Hororata Station, South Island of New Zealand, 43.546°S; 171.898°E, 213 m a.s.l., used record length: NDJFM 1891–2010). See Acknowledgements section for details.

3. Intraseasonal heat waves in SEPG: regional and large-scale anomalies

A total of 460 days satisfy both conditions defined for detecting heat waves (introduced in Section 2). Because many of these days occur in clusters, we select the first day of every group of consecutive days in order to characterize each single event and name that day 'day 0', which also corresponds to the warmest day in the mean signal (see Figures 1 and 3). So defined, we obtain 201 heat waves within the study period, which we consider to be independent. The mean duration of a heatwave cluster, defined here as the number of consecutive days that satisfy the conditions of intensity and persistence, is ∼2.3 days. Note, however, that the warm perturbation typically lasts longer, as shown by the mean signal of the heatwave composite shown in Figure 1(b) (∼2 weeks). Single events within a season are separated by a median (mean) of 20.5 (24.9) days, with a minimum of 4 days and a maximum of 64 days. During 1872–2010 (1900–2010), the mean value of events per season is 1.45 (1.59), with a significant trend of 0.66 events per 100 years at the 95% confidence interval (not significant trend of 0.30 events per 100 years).

3.1. Time evolution of heat waves and sequences of related composites

3.1.1. Heat waves in SEPG

We start by analysing the 21-day composite sequence of T' centred on day 0 (Figure 1(b)) for all heat wave events identified at the SEPG region (Figure 1(a)). T' does not deviate substantially from 0 until day −3, when the values increase sharply and reach a mean anomaly of 4.3 °C on day 0. After day 1, T' decreases less rapidly in comparison to the first half of the sequence (+1.6 K day^{-1} between days −1 and −3 compared with −1.1 K day^{-1} between days 1 and 3, and lower cooling rates thereafter). In fact, the +2 °C anomaly is exceeded between days −2 and 3. Thereafter, positive anomalies over +0.5 °C last almost until day 8. The asymmetry of the T' signal partly reflects the fact that, by definition, day 0 is the first day of a *cluster of days* satisfying the conditions for a heat wave. Thus, after day 0, some persistence of the warm perturbation is observed. A similar asymmetric evolution is observed for z500′ over SEPG (Figure 1(c), red curve). This series shows its maximum amplitude of ∼100 gpm on day −1; that is, it leads the T' series by 1 day. As expected within the development stage of a baroclinic wave, the positive slp′ perturbation, whose sequence depicts mean anticyclonic anomalies over SEPG, leads that of z500′ (T') by 1 day (2 days) (Figures 1(c) and (d), red curves). Oppositely mirroring the slp′ sequence and consistently with the accompanying subsidence conditions, we observe a negative prate′ anomaly in SEPG between days −4 and 1 (Figure 1(e), red curve).

The spatial fields associated with these anomalies are displayed in Figure 2, restricted to the 7-day sequence between days −3 and 3. In the upper row, we observe the intrusion of the anticyclonic anomaly from the southwest into SSA, to the east of the Andes. As noted before, the slp′ maximum is located directly to the east of SEPG on day 0. This anomaly is associated with the development of a temperature dipole in the T' composite (Figure 2, middle row) with warm (cold) anomalies to the south (north) of ∼35°S. The mean T' perturbation exceeding 2 °C over SEPG typically lasts from day −2 until day 3. During this sequence of days, dry anomalies persist in the southern tip of the continent (stronger in southwestern Patagonia), ahead of the anticyclonic anomaly (over the southwest Atlantic), and in southeastern South America (Figure 2, lower row).

Summarizing all, the slp′, T', and prate′ fields show the expected relationships associated with the development of a mid-latitude disturbance. For instance, on day −1, the wet pattern shown by the prate′ field is an imprint of the mid-latitude cyclonic anomaly centred at approximately 40°S; 25°W with SE–NW orientation towards the continent at 20°S. Behind that cyclonic anomaly, the anticyclonic anomaly peaking to the east of SSA seems to drive the dry anomaly ahead of it and the T' increase over the continent. Hence, heat waves in SEPG, large-scale ascent in the SACZ, and large-scale descent in Patagonia (inferred from the prate′ field) are related to the eastward evolution of alternating cyclonic and anticyclonic anomalies. These aspects are further explored in Section 4.

In terms of circulation, we essentially identify three main patterns related to the anticyclonic anomaly that propagates over SSA: on day −3, when the anticyclone is located over the southern tip of the continent, it promotes weak easterly anomalies over the SEPG region; between days −2 and day 0, the anticyclone intensifies while it moves eastward causing northeasterly wind anomalies over SEPG; and, between days +1 and +3, as the anticyclone has moved eastward over the south Atlantic, wind anomalies are very weak over the continent.

The possible drivers of the local heating in SEPG, expressed in the thermodynamic energy equation, are the temperature advection plus adiabatic and diabatic processes. Although a detailed analysis of these terms lies beyond the aims of this work, we first study the radiative effect (one of the diabatic terms) and then the near-surface horizontal temperature advection.

The intraseasonal anomaly of the downward shortwave radiation flux at the surface (Figure 2(a)) exhibits positive values between approximately 37°S and 50°S around day 0. The signal is related to the easterly anomalies of wind at 10 m, which inhibit the moisture advection and the development of cloudiness and precipitation in the western part

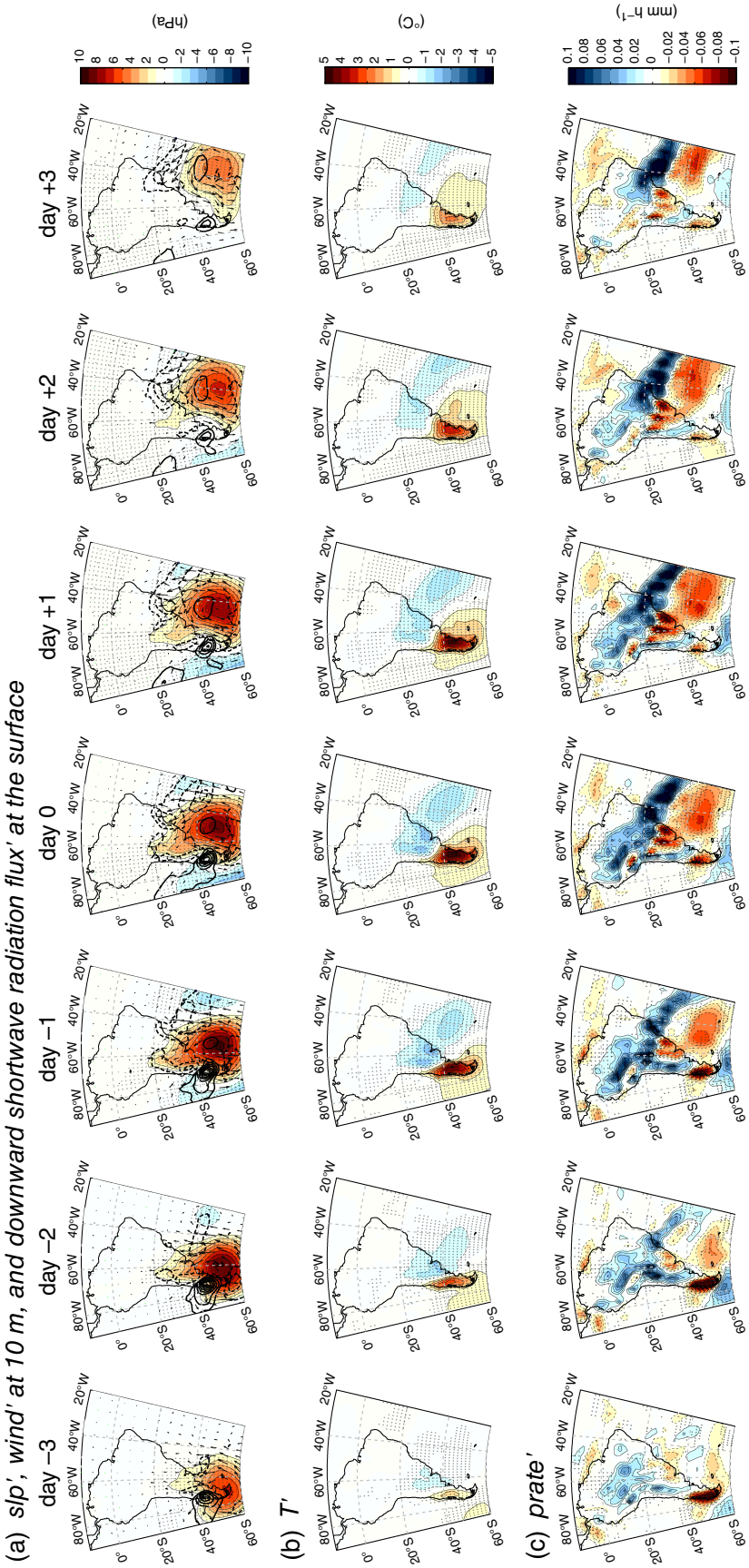

Figure 2. Composite fields of *intraseasonal anomalies* over South America of the 201 heat wave events, centred on day 0, from day −3 until day 3. Upper, middle, and lower panels show the sequences of (a) slp′ (shaded contours every 1 hPa), wind′ at 10 m (vectors), and downward shortwave radiation flux′ at the surface (thick solid/dashed contours for positive/negative anomalies every 10 W m^{-2}), (b) T' (shaded contours every 0.5 °C), and c) prate′ (shaded contours every 0.01 mm h^{-1}). Reddish (bluish) colours and thin solid (dashed) contours denote positive (negative) anomalies (inverse colour scale for prate′); zero contour omitted. Black dots denote values that are statistically significant at 95%; for prate′, a Monte Carlo calculation was made with 500 composites of 201 members.

of the Andes. The positive anomaly of downward radiation flux moves eastward and peaks on day −1 over SEPG, exceeding 60 W m^{-2} around 43°S; 73°W, and decreases towards the Atlantic coast to ∼30 W m^{-2}. These results suggest a positive contribution of the solar radiation to the T' development in the northern part of SEPG. A negative anomaly is observed to the south of 50°S, covering also Tierra del Fuego and peaking over the Drake Passage with values around −25 W m^{-2}. The negative anomalies of downward shortwave radiation fluxes are associated with cloudiness and precipitation (Figure 2(c)). However, given the negative anomaly of this variable in this region, another factor must drive the warming in the southern part of Patagonia.

As shown in Figure S1, Supporting Information, the intraseasonal anomaly of the near-surface horizontal temperature advection exhibits positive values over Eastern SSA, south of ∼43°S, from day −2 onwards. The magnitude of the spatial pattern of this variable is highest on day 0 and increases towards the south with its maximum to the south of ∼50°S. This anomaly of the horizontal temperature advection is mainly driven by its zonal (easterly) component to the north of ∼50°S and by its meridional (northerly) component to the south of ∼50°S.

In summary, in connection with the development of intraseasonal heat waves in SEPG, we observe an enhanced downward shortwave radiation flux in the northern part of Patagonia (between ∼37° and ∼50°S) and warm horizontal temperature advection over most of Patagonia (south of ∼43°S).

3.1.2. Robustness of the heat wave temperature signal in 20CRv2

We assess the robustness of the 20CRv2 heat wave signal from SEPG by comparing it with instrumental mean temperature ($T_m{}'$) anomalies for 1957–2010 from Comodoro Rivadavia Aero and Río Gallegos Aero (described in Section 2; see Figures 1 and 3), which were obtained in the same way as the intraseasonal time series from the reanalysis. The statistics of the comparison between 20CRv2 and the station data is shown in Table 2. Figure S2 shows the mean T' composite for heat waves from SEPG (shown in Figure 1(b)) together with the composite calculated for the closest gridpoint to each of both stations, as well as the instrumental time series. The mean instrumental $T_m{}'$ heat wave signal of Comodoro Rivadavia shows a warm bias of ∼1.5 °C on day 0 with respect to 20CRv2. Nevertheless, the general evolution of the instrumental anomalies is well reproduced by the reanalysis, in particular regarding the timing of the T' maximum on day 0. Concerning their magnitude, the measurements taken at Río Gallegos are in better agreement with the reanalysis. The instrumental $T_m{}'$ peak is recorded here on day −1 and not on day 0 as in 20CRv2, a result that suggests a northward propagation of the T' signal related to heat waves in SEPG within Patagonia.

It is worth commenting that nearly 35% of the heat wave events found for SEPG using 20CRv2 for SEPG are related

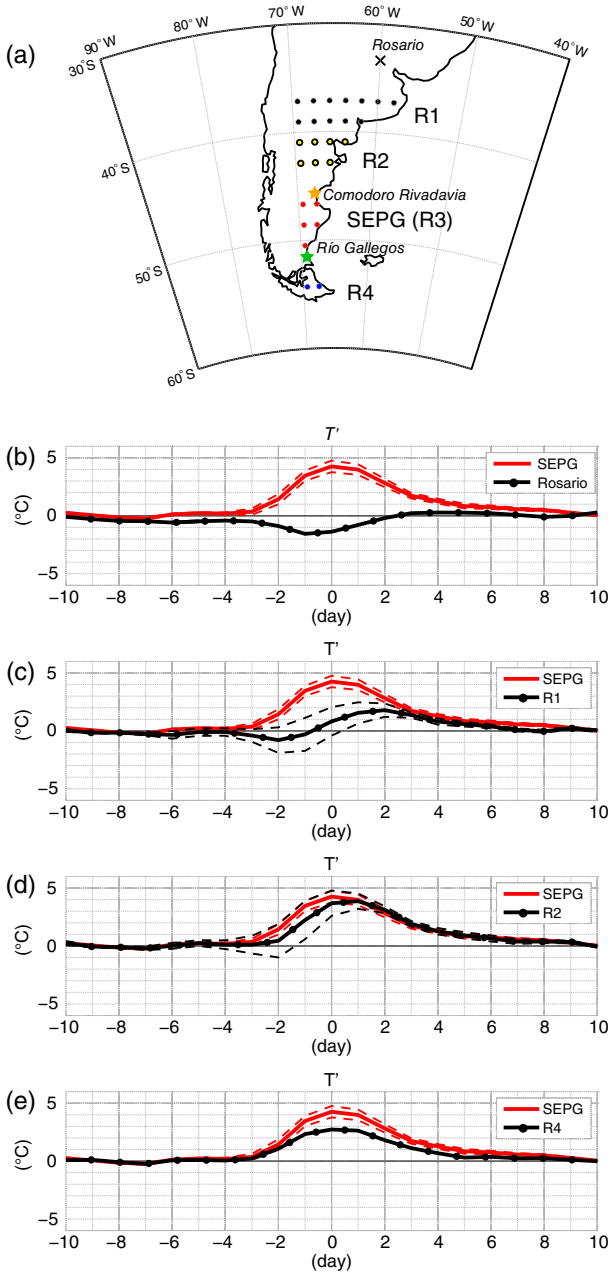

Figure 3. (a) Gridpoints (20CRv2) considered within SEPG/R3 (red, 46°–52°S; 65°–70°W) and regions R1 (black 36°–39.5°S, east of 70°W), R2 (yellow, 40°–44°S, east of 70°W) and R4 (blue, 53°–55°S, east of 70°W). The nearest gridpoint to Rosario Aero Station (32.92°S; 60.78°W) is marked with an *x*. (b–e) 21-day mean time series of T' in SEPG (red curve) and Rosario, R1, R2, and R4 (black curves), respectively, centred on day 0, calculated from the 201 heat waves in SEPG. Solid (dashed) curves correspond to the composite spatial mean (standard deviation) of the corresponding regions.

to cases where the instrumental absolute T_x is above its 99% percentile in Comodoro Rivadavia. Although the SEPG signal extracted from the reanalysis is not necessarily representative of any single gridpoint or station location, this result and the relative good agreement between 20CRv2 and the instrumental observations seem to indicate that such very extreme instrumental warm cases are not necessarily persistent enough to be considered as intraseasonal heat waves.

Table 2. Evaluation statistics (biasses and correlation coefficients) of the temperature records of Comodoro Rivadavia and Río Gallegos (see Figure 3(a)) with respect to the temperature time series extracted from their closest gridpoints in 20CRv2 (ensemble average of mean temperature).

	T_n		T_x		T_m	
Station	Abs.	IS	Abs.	IS	Abs.	IS
Comodoro Rivadavia	−3.73/0.64	−0.01/0.62	8.57/0.64	−0.01/0.63	2.42/0.71	−0.01/0.69
Río Gallegos	−2.41/0.59	0.00/0.56	9.70/0.63	0.00/0.61	3.67/0.69	0.01/0.67

Values for instrumental minimum temperature (T_n), maximum temperature (T_x), and mean temperature (T_m) are shown. The bias (°C) and the correlation coefficient are calculated with respect to the ensemble mean of 20CRv2 and are shown for the instrumental absolute values (abs.) and their intraseasonal (IS) anomalies. The period of reference is 1957–2010.

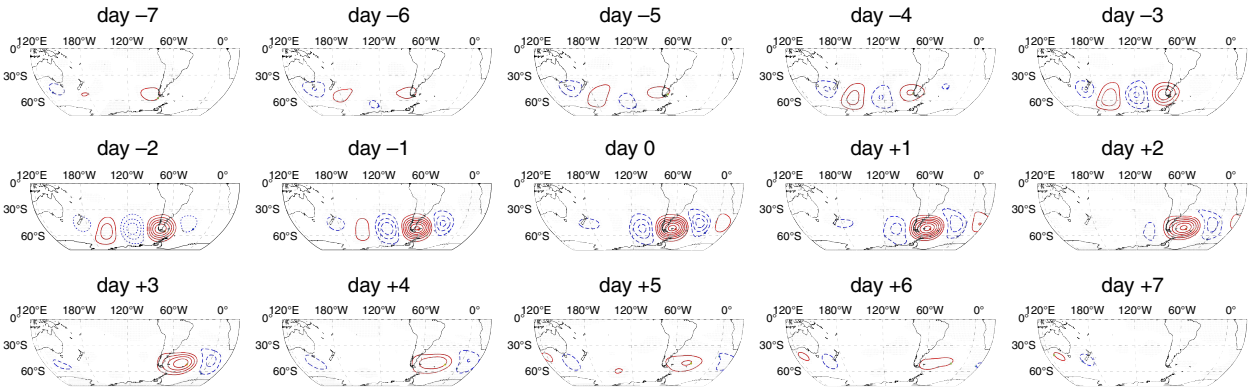

Figure 4. Composite fields of z500′, considering the 201 heat wave events, centred on day 0, shown from day −10 until day 10. Solid red (dashed blue) contours are drawn every 20 gpm and denote positive (negative) anomalies; zero contour omitted. Statistically significant anomalies at 95% are depicted by black dots.

3.1.3. Regional dynamics associated with heat wave occurrences in SEPG

The regional circulation dynamics associated with the heat waves at SEPG are analysed using 20CRv2, through the definition of neighbouring regions of SEPG and the comparison of their T' evolution. As shown in Figure 3(a), these four regions correspond (from north to south) to the closest gridpoint to Rosario Aereo (32.92°S; 60.78°W, whose intraseasonal heat wave signal was analysed by Cerne and Vera (2011)), and to regions formed by the gridpoints located within zonal bands to the east of 70°W: R1 (36°–39.5°S), R2 (40°–44°S), and R4 (53°–55°S). SEPG corresponds here to R3. Figure 2(b) previously showed that the T' signals from the R1–R4 regions are affected by the passage of the same baroclinic disturbance. The temporal evolution of the regional T' composites are shown in Figure 3(b)–(e). In R4, to the south of SEPG, the warm anomaly begins almost synchronously with that of SEPG, due to the meridional temperature advection caused by the anticyclonic circulation depicted in Figure 2(a). The warming in R4 shows a lower magnitude than in SEPG and reaches a maximum of nearly 3 °C on day 0. The lags observed in R2, R1, and Rosario indicate that the T' anomaly propagates from South to North. The magnitude of the warm anomaly in R2 is comparable with that of the heat wave in SEPG, which lies directly to its south. Although the onset of the event in R2 occurs later than in SEPG, after day 0 both signals evolve similarly, and thus the local warm perturbation lasts less than in SEPG. In R1, we observe a cold perturbation on day −2 associated with the cold advection promoted in that region by the southeasterly wind anomaly induced by the anticyclone. This signal evolves later into a local warming anomaly, reaching a moderate maximum of nearly 2 °C on day 2. Further north, next to Rosario, we just recognize a cold perturbation that is almost in phase with the heat wave signal from SEPG. This subtropical cooling corresponds to the temperature dipole pattern induced by the trough-ridge system.

3.2. The wave train pattern over the South Pacific

In this subsection, we analyse the mid-level circulation anomalies associated with intraseasonal heat waves in SEPG on the hemispheric scale. They are described by the intraseasonal anomalies of geopotential height at 500 hPa, i.e. z500′. The 15-day sequence of z500′ composites over the South Pacific Basin centred on day 0 (Figure 4) shows on day −7 a negative height anomaly to the south of SE Australia and a positive anomaly to the SE of New Zealand. From that day onwards, we observe both features moving eastward from Oceania with a phase speed of around 6–7° per day, embedded in a developing wave train pattern extended along the South Pacific. On day −4, the negative anomaly observed on day −7 to the south of SE Australia is located over the Southern Island of New Zealand and persists in that position over the next days

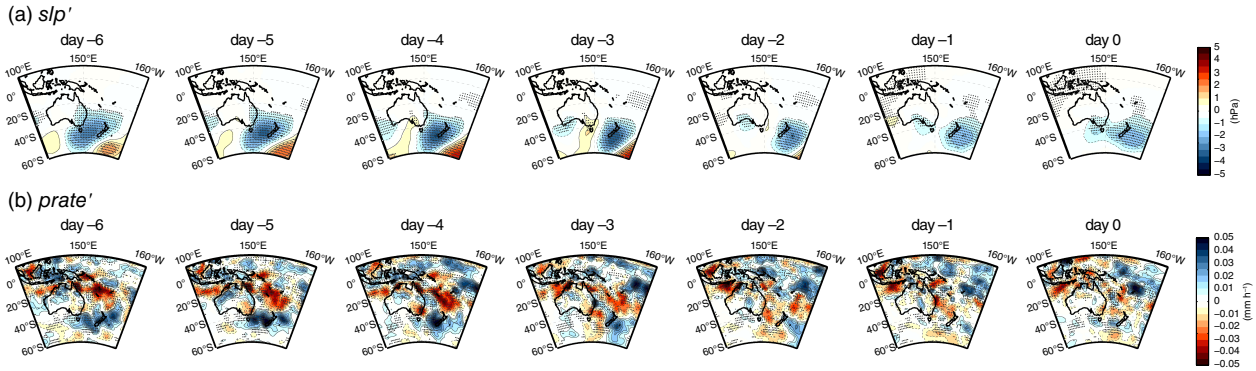

Figure 5. Composite fields over Oceania based on the 201 heat wave events at SEPG, centred on day 0, shown from day −6 until day 0. Upper and lower panels show the sequences of (a) slp′ and (b) prate′, respectively. Reddish (bluish) colours and solid (dashed) contours denote positive (negative) anomalies (inverse colour scale for prate′). Contours every 0.5 hPa and 0.005 mm h^{-1}; zero contour omitted. Black dots denote values that are statistically significant at 95%; for prate′, a Monte Carlo calculation was made with 500 composites of 201 members.

while its intensity decays. At the easterly edge of the wave train, we observe a strengthening ridge over the southern tip of South America. On day −1, the positive centre is located to the east of SSA and reaches its peak intensity. By day +3, the anticyclonic anomaly is centred over the southwest Atlantic and progressively weakens.

It is worth to comment that this anticyclonic anomaly, which will induce the heat waves in SEPG, progresses very slowly from its location to the west of the southern tip of the continent on day −5 to day +4, when it is found off the eastern coast of SSA. Essentially, a 2-wave packet is discernible all along the evolution of the large-scale pattern, although different waves determine it. Between day −1 and day 0, the upstream wave decays while a new wave develops downstream. This could be an evidence of *downstream baroclinic development*, a process that has been identified in previous works (Lee and Held, 1993; Orlanski and Chang, 1993).

The z500′ composites suggest a relationship between the heat wave signal in SEPG and the circulation in the South Pacific and over Oceania. Similar wave trains linking the climate variability over the western south Pacific region with that over South America have been previously identified on interannual timescales (e.g. Berman *et al.*, 2013) and also on intraseasonal timescales (e.g. Liebmann *et al.*, 2004). The spatial structure of the z500′ pattern together with the source region of the anomalies strongly insinuates that the Madden–Julian Oscillation (MJO, Madden and Julian (1971)) might be involved in its triggering. Indeed, the MJO is the leading intraseasonal variability mode within the tropics. It consists of a perturbation in the atmospheric circulation and in deep convection that propagates eastwards, and is associated with temperature and precipitation anomalies not just in the tropical band, but also beyond it through teleconnection patterns (Zhang, 2005, 2013). Alvarez *et al.* (2015) extensively described the influence of the MJO in both SAT and precipitation in South America. The complete analysis devoted to the modulation of SAT in Patagonia and its relationship with the occurrence of heat waves in SEPG is the focus of a further study of the same authors of present paper (Jacques-Coper *et al.*, 2015).

We also explore the teleconnection that consists in the anticorrelation pattern between temperature anomalies in SSA and precipitation anomalies in SE Australia on the interannual timescale (Jacques-Coper and Brönnimann, 2014). A more profound understanding of this teleconnection might be useful as a further source of validation of the remote signals associated with the heat wave events in SEPG. Figure 5 shows the slp′ and prate′ composites for Oceania based on the heat wave events identified at SEPG, displayed between day −6 and day 0. In correspondence with the eastward propagation of a slp′ cyclonic anomaly over the Tasman Sea, we identify a dry (wet) pattern over SE Australia (South Island of New Zealand) that peaks around day −4. Positive prate′ anomalies are observed over the North Island of New Zealand until day −5. These signals, showing dry conditions in SE Australia and wet conditions over New Zealand by day −5, are well captured in the time series of Figure 1(e). The dry anomaly in SE Australia during the first days of the evolution seems then to be caused by the cyclonic circulation over the Tasman Sea. Relatively dry air masses are transported eastward from the Australian continent to the Sea, which is the opposite pattern of the easterly anomaly that typically leads to precipitation over that region (Rakich *et al.*, 2008). Contrastingly, relatively moist air masses are advected by this system from the west towards New Zealand, inducing the local wet anomaly, in agreement with Ummenhofer and England (2007).

As a means to validate our results, we use meteorological observations from SE Australia and New Zealand to analyse the precipitation probability perturbations related to the heat wave events identified for SEPG in 20CRv2. For that, we use composites of 21-day sequences of precipitation, centred on day 0. The methodology followed for calculating the rain probability perturbations and the corresponding results are described in the Appendix.

4. The heat wave events and the SACZ

Cerne and Vera (2011) showed that summer heat waves in Rosario (Figure 3) are strongly influenced by the SACZ

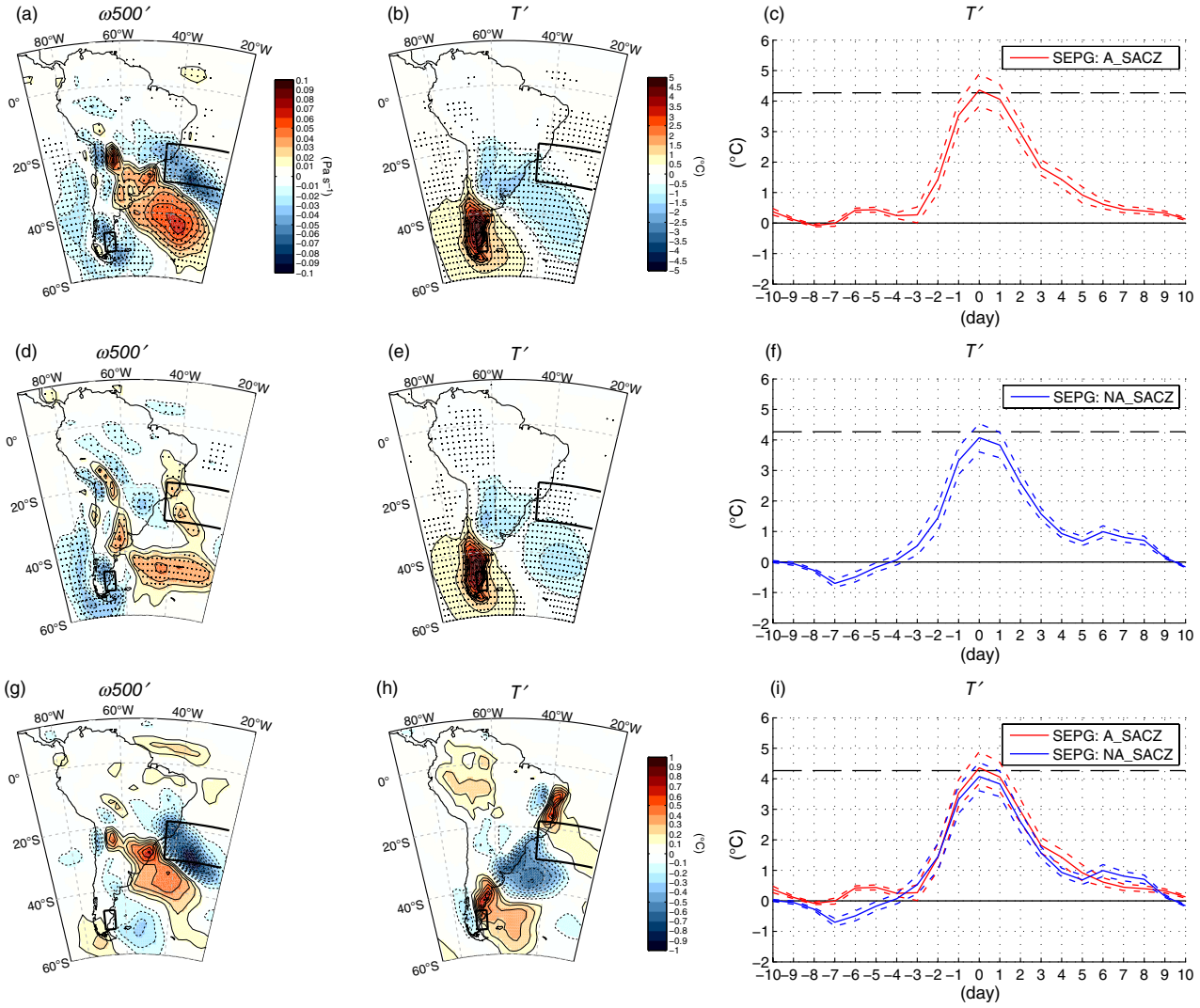

Figure 6. Composites of (a,d,g) $\omega 500'$ and (b,e,h) T', and (c,f,i) 21-day T' sequences centred on day 0 for: (a–c) the 135 active SACZ (A_SACZ) cases and (d–f) the 66 non-active SACZ (NA_SACZ) cases, from the total of 201 heat wave events in SEPG; (g–i) difference fields between A_SACZ and NA_SACZ. Interval units are 0.01 Pa s^{-1} for $\omega 500'$ and 0.5°C for T' (0.1°C for panel h).

dynamics. Enhanced convection in the SACZ (i.e. an active SACZ) induces subsidence over the region around Rosario and thus reinforces the local temperature rise through adiabatic warming and diabatic processes. The sub-monthly (2–30-day range) variability of the SACZ is related to a nearly equivalent barotropic wave train circulation pattern over the South Pacific (Liebmann *et al.*, 1999), a feature that resembles the results presented in this study. Moreover, Lima *et al.* (2010) found a well-defined wave train over the south Pacific and South America, with a strong ridge over Argentina and active SACZ conditions in association with heavy rainfall episodes in southeast Brazil. Indeed, a remote manifestation observed in connection with the heat waves in SEPG is a wet anomaly signal in the SACZ from day −2 onwards (Figure 2(c)). Because the SACZ, a quasi-stationary system, is related to several climate impacts in South America, as shown above, it is of interest to explore to which extent the intraseasonal variability of convection in that region is linked to the development of heat waves over SEPG.

To investigate the connection between the SACZ and the heat waves in SEPG, we define a SACZ index as the spatial mean value of the $\omega 500'$ anomalies within 18°–30°S; 20°–44°W (Figure 1(a)). For this definition, as in Cerne and Vera (2011), we use anomalies that result from subtracting the seasonal cycle from the raw values but retaining the interannual anomalies. We classify the daily SACZ activity based on the area-mean sign of these local $\omega 500'$ anomalies. Hence, an active (non-active) SACZ corresponds to abnormal ascent (descent) conditions determined by negative (positive) $\omega 500'$ anomalies spatially averaged over the SACZ region (Figure 1(a)), and is hereafter abbreviated as A_SACZ (NA_SACZ).

The dynamical conditions associated with heat wave events in SEPG and further discriminated by the SACZ activity are shown in Figure 6. Our results show that 135 out of the 201 heat wave events (67.2%) occur during active SACZ periods. As shown in Figure 6(a), these cases exhibit an enhanced ascent band in the SACZ region and a subsidence area over southeastern South America (at

around 30°S); both anomalies are oriented in the NW–SE direction and extend well into the southwest Atlantic. Also weak ascent is observed over the southern tip of the continent. In contrast, non-active SACZ cases (Figure 6(d)) imply very weak subsidence over the SACZ, suppressed subsidence over subtropical South America and the southwest Atlantic (spatially more restricted than in the previous case) and ascent again over southern Patagonia. As a consequence, the $\omega 500'$ difference field (Figure 6(g)), calculated as A_SACZ – NA_SACZ, shows a similar ascent–subsidence–ascent pattern as for the A_SACZ cases, although no signal is detected over SEPG. Thus, we can only infer that stronger heat waves are related to stronger $\omega 500'$ anomalies over the southern half of South America. No significant upstream effect of the SACZ on SEPG can be identified.

The corresponding z500′ sequences (not shown) reveal stronger anomalies within the wave train pattern in the South Pacific in connection with the A_SACZ events. In particular, the anticyclonic anomaly over SSA appears sooner and is more pronounced in the A_SACZ composite than in the NA_SACZ one. This feature seems to slightly enhance the warming observed before at the peak of the heat wave (day 0) for the A_SACZ composite with respect to the NA_SACZ composite (Figure 6(i); T' differences of +1.8 °C on day −6 and +0.3 °C on day 0).

5. Possible relationships between the intraseasonal circulation anomalies and the interannual and decadal timescales

In this section, we analyse a possible link between the intraseasonal heat wave events in SEPG and the interannual variability of the DJF temperature means (summer-to-summer variability). For that, we use the DJF mean SAT anomaly time series over SEPG (1878–2004), from which the interdecadal variability has been previously removed (calculation described in Section 2). Extreme warm (cold) summers are defined as those whose seasonal SAT mean exceeds one positive (negative) long-term summer-to-summer standard deviation (0.63 °C within 1878–2004). We found that 23 (28) heat waves occur during 12 (14) extreme warm (cold) summers (see Table 3). That is, these 12 (14) extreme warm (cold) summers, which correspond to 9.4% (11.0%) of the total record length of 127 years, account for 11.4% (13.9%) of the total 201 heat wave events. Therefore, heat waves do not tend to concentrate in years with extreme seasonal means.

The relationship to be analysed between both timescales is the spatial structure of the wave train patterns leading to heat waves in SEPG in positive and negative extreme years. Figure 7 shows the wave train pattern observed on day 0 for the composite of (1) all 201 heat waves, (2) 23 heat waves within extreme positive summers, and (3) 28 heat waves within extreme negative summers, and their respective difference fields. The anomaly field of extreme warm summers compared with all events (Figure 7(b), black contours) indicates that the wave train associated with this group exhibits stronger positive values south of Australia, as well as south of 60°S next to the Ross Sea (around the date line), and off Dronning Maud Land in Antarctica (at the Greenwich Meridian). For this composite, we also observe a strengthened western flank of the anticyclonic anomaly over SSA, whereas the cyclonic anomaly located to its west, in the southeast Pacific, is weaker than in the composite of all events. Moreover, there is also a stronger cyclonic anomaly in the south Atlantic (the one related to the SACZ), and also south of South Africa. In contrast, in association with extreme cold summers (Figure 7(c)), the composite wave train pattern seems to be more zonal-shaped and also meridionally more restricted (within ~30°S and 60°S) than the one of the warm years (Figure 7(b)). Moreover, within the cold

Table 3. Heat waves identified within warm and cold summers.

23 heat waves within 12 warm summers				28 heat waves within 14 cold summers				
1923 (1)	1944 (3)	1962 (2)	1979 (2)	1910 (2)	1951 (3)	1966 (3)	1977 (2)	1992 (3)
1926 (1)	1952 (1)	1963 (3)	1984 (3)	1947 (3)	1956 (1)	1971 (1)	1981 (2)	1996 (2)
1931 (2)	1960 (1)	1978 (2)	1985 (2)	1948 (1)	1959 (2)	1972 (1)	1988 (2)	

The number of events per season is indicated in brackets.

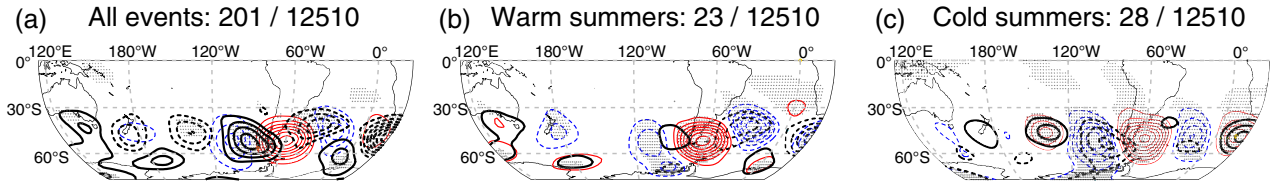

Figure 7. Composites of z500′ considering heat waves within (a) 1872–2010 ($n = 201$), (b) 12 extreme warm summers ($n = 23$), and (c) 14 extreme cold summers ($n = 28$); thin solid red/dashed blue contours denote positive/negative values every 20 gpm; zero contour omitted. For (b) and (c), see Table 3. The difference fields of the spatial structures of the aforementioned groups are also shown: (a) extreme warm summers – extreme cold summers, (b) extreme warm summers – all events, and (c) extreme cold summers – all events; thick solid black/dashed black contours denote positive/negative difference values every 20 gpm; zero contour omitted. Black dots indicate the statistical significance of the difference fields at 95%.

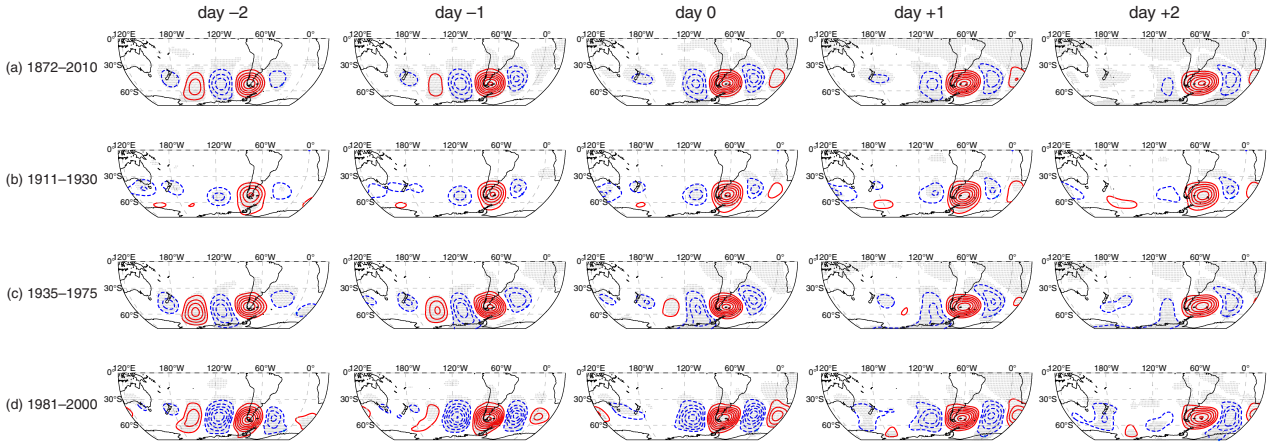

Figure 8. Sequence of composite fields of z500′ between day −2 and day 2 considering heat wave events within (a) 1872–2010 (201 events), (b) 1911–1930 (27 events), (c) 1935–1975 (69 events), and (d) 1981–2010 (49 events). Solid red (dashed blue) contours every 20 gpm denote positive (negative) anomalies; zero contour omitted. Statistically significant anomalies at 95% are depicted by black dots.

composite, while no cyclonic anomaly can be seen over New Zealand, we observe an anticyclonic anomaly around 45°S; 140°W. Furthermore, in this composite, the cyclonic anomaly in the southeast Pacific (upstream of SSA) is stronger than in the previous composites, whereas the cyclonic anomaly in the south Atlantic (downstream of SSA) is located more to the south. South of South Africa, an anticyclonic anomaly is found for this cold summers group. Consequently, the difference between warm (positive) and cold (negative) extreme summers (Figure 7(a), black contours) exhibits positive anomalies to the south of Australia, over the Ross Sea, to the west of SSA, and off Dronning Maud Land in Antarctica. In turn, negative anomalies are observed over New Zealand, at 45°S; 140°W, in the south Atlantic, and south of South Africa. We conclude that, within extreme warm summers, the slp′ anomaly related to the action centre over SSA and the southwest Atlantic tends to be slightly shifted to the west than those of the composites of extreme negative years and of all events. Moreover, the mean wave train pattern for cold summers seems to exhibit a more zonal pattern than that of the warm summers. Thus, the group of heat waves within extreme warm summers tends to resemble more the composite of events found for active SACZ.

Another aspect worthy of being investigated in long-term reconstructions is the possible temporal variation of the spatial structure of the wave train pattern identified in z500′ in association with heat wave events in SEPG. It is important to point out that geopotential heights at 500 hPa are derived in the 20CRv2 data set from observations of surface pressure only, which are combined with background first-guess fields supplied by global model forecasts (Compo *et al.*, 2011). Therefore, considering the important deficiencies in the observation spatial coverage in the Southern Hemisphere, particularly during the early decades, the geopotential height fields are model-dependent. Thus, caution should be taken in the conclusions that emerge from these fields.

The interdecadal summer SAT variability in SSA is dominated by a mode that is correlated to the Pacific Decadal Oscillation (PDO) since the 1960s but appears to be out of phase with it during the first decades of the 20th century (Jacques-Coper and Brönnimann, 2014). This main interdecadal variability mode defines warm decadal periods between early 1910s and early 1930s and between late 1970s and mid-1990s, and a cold period amid them. Therefore, we compute separate composites of z500′ associated with heat wave events in SEPG for the following sub-periods: 1911–1930, 1935–1975, and 1981–2000. The number of heat waves (n) within each of these three periods are $n = 27$ or 1.35 events year^{-1}, $n = 69$ or 1.68 events year^{-1}, and $n = 49$ or 2.45 events year^{-1}, respectively. The corresponding z500′ composites, along with the composite computed for the whole period, 1872–2010, are shown in Figure 8, spanning between day −2 and day +2 from day 0. The arch shape of the z500′ wave train pattern during 1872–2010 resembles better the composite of the cold multidecadal period 1935–1979 than those of the warm periods 1911–1930 and 1981–2000, which exhibit more zonal patterns. Besides, during 1981–2000, which was a relatively warm period within SEPG in particular for summer (Jacques-Coper and Garreaud, 2014), a higher frequency of events per year is registered and their associated z500′ anomalies appear stronger than during the preceding periods.

A conclusive explanation to these observations lies beyond the scope of this study and modelling work should be performed in order to address these aspects, in particular regarding how the climate background state, partly linked to the large-scale low-frequency variability (e.g. the PDO and global warming), might affect the occurrence of extreme events such as heat waves in Patagonia. However, we suggest some links to previous results that could be of interest for further research. The positive phase of the Southern Annular Mode (SAM), a mode with a broad variability spectrum, is associated with warm conditions in SSA (Gillett *et al.*, 2006; Garreaud *et al.*, 2009). Moreover, a strong positive trend of the SAM index, observed since mid-1970s (Thompson and Solomon, 2002; Marshall, 2003), has been related to a southward shift of the

mid-latitude storm track and to the poleward shift of frontal activity in the Southern Hemisphere, mainly during the warm season (Solman and Orlanski, 2013). These observations are consistent with the more zonal-shaped wave train pattern observed during 1981–2000 in Figure 8(d), which does not clearly show the equatorward deflection over South America and the south Atlantic observed for the other periods. There are many possible implications of this change on the orientation of the waveguide since mid-1970s, including those related to disruptions of teleconnections between Oceania and South America (Jacques-Coper and Brönnimann, 2014) and also between South America and South Africa (Compagnucci *et al.*, 2002). However, no similar explanation for the more zonal shape of the wave train pattern during the first warm period 1911–1930 is evidently linked to a concurrent positive trend of the summer (DJF) SAM index (Jones *et al.*, 2009; Abram *et al.*, 2014).

6. Summary and conclusions

We have analysed the occurrence of summertime heat wave events in SEPG since the late 19th century using the 20CRv2. A total of 201 heat wave events were identified for 1872–2010. The associated regional intraseasonal anomalies of temperature (T') affect a broad area in SSA on both sides of the Andes.

Local instrumental SAT records show that 20CRv2 captures the timing and structure of intraseasonal heat waves in SEPG. Their evolution is described by the 21-day composites of various variables centred at day 0. This day corresponds to the first day of a cluster of days that satisfy the conditions of intensity and persistence which define a heat wave. Moreover, day 0 coincides with the T' peak of 4.3 °C. The temperature increase is observed from day −3 onwards, and the warm anomaly then typically lasts until day 10. The positive perturbation of slp′ peaks at day −2 over SEPG and decays thereafter. Local warming is hence related to the eastward drift of a surface anticyclone, which is situated to the east of SEPG at day 0. In agreement with the baroclinic structure of this perturbation on the eastern side of the Andes, z500′ reaches its highest value over SEPG on day −1. As a consequence of these circulation anomalies, a dry anomaly is observed in SSA between days −4 and 1. A typical heat wave in SEPG is accompanied by a regional warming effect throughout Patagonia, which is first observed at the southern tip of the continent and propagates northward. Moreover, at subtropical latitudes, these events are related to moderate cooling. This fact explains the resemblance between the sequence of fields presented here and those associated with the intrusion of cold air over subtropical South America by Garreaud (2000). Thus, we have extended the results of that study into a subcontinental context and have complemented it with a perspective on the associated large-scale circulation anomalies.

Our findings show that heat waves in SEPG are related to large-scale circulation anomalies that are visible at least 1 week in advance in the South Pacific. Although previous studies (e.g. Cazes-Boezio *et al.*, 2003; Robertson and Mechoso, 2003) did not find recurrent circulation regimes there during summer, we do see that they appear in connection to extreme temperature events in SSA. Based on this result, we also explored climate signals in Oceania that co-occur with the heat wave events in SEPG. We found in 20CRv2 that the anticyclone that precedes a heat wave over SEPG is also related to a cyclonic anomaly over the Tasman Sea. Both circulation anomalies are embedded in a quasi-stationary wave-train-like pattern with negative (positive) action centres in New Zealand and to the west of South America (north of the Ross Sea and SSA). The cyclonic anomaly over the Tasman Sea propagates eastward from a position south of SE Australia on day −6 and reaches New Zealand on day −4, inducing dry conditions in the former region and a wet anomaly in the latter one, a result confirmed by century-long instrumental records. The wave train pattern is evident from day −6 onwards and resembles the structure described for the interannual summer SAT variability in Eastern SSA by Jacques-Coper and Brönnimann (2014), who showed an anticorrelation between precipitation in southeastern Australia and SAT in Eastern SSA. Hence, this result provides an explanation for the origin of the said teleconnection at intraseasonal and interannual timescales.

The analysis on the source of this wave train pattern is beyond the goals of this study. However, its relationship with the MJO is further explored in an additional paper by the same authors of the present contribution (Jacques-Coper *et al.*, 2015).

Two thirds of the heat wave events in SEPG are related to convective conditions in the SACZ, although no evident upstream effect can be identified in SEPG considering the anomalies induced by the wave train pattern. The corresponding circulation anomalies shown in this study are similar to those related to the summer sub-monthly activity of the SACZ, a quasi-stationary system (Liebmann *et al.*, 1999; Lima *et al.*, 2010). Moreover, Carvalho *et al.* (2002) found ascent conditions over the southwest Atlantic that are similar to the fields shown in this work in connection with a *weak-oceanic* pattern of outgoing longwave radiation anomalies in the SACZ. This pattern induces extreme precipitation events in the coastal region of southeast Brazil, a result that is also consistent with the precipitation composites shown in the present paper. Hence, our findings provide a continental context not just for temperature but also for precipitation impacts related to subseasonal wave-train-like circulation anomalies over the South Pacific and South America.

Finally, we proposed a link between the wave train pattern anomalies on intraseasonal, interannual (summer-to-summer), and decadal timescales. We found that intraseasonal heat waves occurring in extreme warm summers (i.e. in years with strong positive seasonal SAT means) show a less zonal wave train pattern of geopotential height at 500 hPa (resembling more the *active SACZ* case), and that they are related to slightly westward-shifted positive z500′ over SSA than those occurring in extreme negative years (i.e. in years with strong negative seasonal SAT means). The decadal modulation of the wave train

pattern, as well as the interaction between timescales regarding this feature, might be analysed in more detail in further works.

The findings presented in this study unveil regional and large-scale processes related to intraseasonal SAT perturbations in SEPG. Besides, our results suggest a potential link between synoptic-to-intraseasonal phenomena and previous results on the main interannual and interdecadal SAT variability modes of SSA. The use of independent instrumental data adds robustness to this study and provides a means of validation of 20CRv2 in the Southern Hemisphere. In particular, the signal found in century-long daily precipitation records from Oceania confirms the teleconnection between this region and SEPG. Modelling studies could aim at exploring dynamical features related to open issues raised by this study, such as the origin of the wave train pattern linked to the heat waves in SEPG and its interdecadal modulation.

Acknowledgements

Twentieth century reanalysis V2 data were provided by the NOAA/OAR/ESRL PSD, Boulder, Colorado, USA (http://www.esrl.noaa.gov/psd/). Rainfall data from New Zealand are available at the New Zealand National Climate Database (http://cliflo.niwa.co.nz/). Precipitation data from Australia were obtained from the Australian Bureau of Meteorology (http://www.bom.gov.au/climate/data/). We would like to thank Aldo Montecinos and two anonymous reviewers for their useful comments, which improved this work. MJC thanks also Félix Carrasco, Paulina Gajardo, and Aldir Polymeris for their support. MJC acknowledges the CLIMANDES project (SDC, Switzerland) and the BecasChile scholarship program (Comisión Nacional de Investigación Científica y Tecnológica de Chile, CONICYT). CV and BC acknowledge the ANPCyT PICT-2010-2110 Project (Argentina).

Appendix

Calculation of precipitation probability perturbations in Oceania

In order to compute the precipitation probability perturbations for stations of SE Australia and New Zealand, related to heat wave events in SEPG, we first define a mean precipitation *background probability* from the climatology. For each of the analysed precipitation records, we identify daily rainy events from November to March during the period 1961–1990 according to the thresholds 1 and 10 mm. Each day is assigned a 1 in case of precipitation excess of a given threshold and a 0 otherwise. Thus, for each threshold, the *background probability* of rain for every Julian day within this period corresponds to the 30-year average of this binary classification.

Then, we compute the local precipitation signal associated with heat wave events in SEPG. For every rainfall record and precipitation threshold, we form 21-day binary rainfall sequences associated with each heat wave event in SEPG that overlap the rainfall data (i.e. a total number of 201 sequences or less), centred on day 0. One should note that the heat wave events may partly fall within the reference period (1961–1990). The mean probability of rain for each day within these sequences is calculated again as an average, i.e. the number of rainy events on a certain date within the sequence composite divided by the total number of heat waves considered. For each precipitation record, this results in a rain probability sequence of 21 days associated with heat wave events, centred on day 0, called hw_{rpbb}.

The next step is to calculate the probability of rain that a sequence of 21 days centred on the same Julian days as those of the heat waves (day 0) would have if they were referenced to the norm, i.e. within the *background probability* of 1961–1990. This results in a sequence of mean probability of the composite calculated from the norm, which we denominate $norm_{rpbb}$.

Finally, the sequence of probability perturbations associated with heat wave events compared with the climatological *background probability* is simply given by

$$\Delta_{\mathrm{rpbb}} = hw_{\mathrm{rpbb}} - norm_{\mathrm{rpbb}} \tag{A1}$$

So defined, Δ_{rpbb} represents the mean local change of rain probability for every day of the sequence centred on day 0, i.e. the mean heat wave, in comparison to the reference period 1961–1990.

We assess the robustness of this signal through Monte Carlo realizations. For each station, we select 1000 composites of 201 21-day sequences centred on random days from the whole precipitation record. We then repeat the aforementioned procedure to calculate the sequence of mean probability perturbations associated with these groups of random events. This results in a distribution of probability perturbation values for each one of the 21 days of the sequence. In the end, we compare Δ_{rpbb} with the sequence of means of those distributions, and also with the sequences of the 25 and 75% percentiles.

Figure S3 shows the probability perturbations of precipitation computed for SE Australia (Cataract Dam Station, upper panel) and the South Island of New Zealand (Hororata Station; lower panel) in association with heat wave events in SEPG. Black (white) bars represent the probability perturbations computed for each day of the sequence, associated with precipitation in excess of 1 mm (10 mm). Blue (red) curves show the mean and 25 and 75% percentiles of the Monte Carlo distributions for those thresholds. In SE Australia (Figure S3(a)), we observe almost only negative perturbations, i.e. less probability of rain in this area, in connection with heat waves in SEPG. In particular, for events above 1 mm, we identify *dry conditions* between days −10 and 3, and 8 and 10 and a *wet cluster* in-between, from day 4 until day 7. The perturbation in rain probability related to events exceeding 10 mm follows a similar behaviour. Compared with the 1 mm events, in this case the probability differences are mostly lower due to the also lower frequency of these stronger events (Table S1). The fact that the mean distribution of the random sequences is negative points to the wet bias and the

higher probability of rain exceeding the defined thresholds in this region during the reference period 1961–1990 in comparison with the whole period (Table S1).

In turn, the record from the South Island of New Zealand (Figure S3(b)) exhibits positive probability perturbations of rain events above 1 mm, i.e. *wet conditions*, between days −10 and 0, with a peak on day −5, and again on day 7. Although the signal associated with rain events larger than 10 mm follows a similar pattern, it shows much lower amplitude, reflecting again the fact that these events are less frequent than those exceeding 1 mm (Table S1). The little positive departure from zero of the random 1 mm signal is not caused by a mean precipitation bias of the reference period 1961–1990 compared to the whole period, but apparently by the fact that the rain probability associated with events exceeding this threshold is lower during 1961–1990 (Table S1).

We conclude that the precipitation probability perturbations in SE Australia and New Zealand, detected in instrumental records from both regions and concurrent with the occurrence of heat wave events in SEPG, confirm the prate′ signals found in reanalysis data (Figure 1(e), cyan and green curves). Therefore, they provide a means for a remote validation of the robustness of the heat wave and teleconnection signals detected in 20CRv2.

Supporting Information

The following supporting information is available as part of the online article:

Figure S1. Composite fields of intraseasonal anomalies of temperature advection at 925 hPa around day 0, from day −2 until day 2, considering the 201 heat wave events (contours every 2×10^{-6} K s^{-1}): (a) zonal component, (b) meridional component, and (c) total horizontal temperature advection (sum of the zonal and the meridional component). In all panels, wind′ at 10 m is also plotted (as in Figure 2(a)).

Figure S2. 21-day composite sequences of T' from 20CRv2 and the instrumental records, associated with the 201 heat wave events in SEPG identified in 20CRv2, centred on day 0: SEPG mean (grey curve, 20CRv2, 1872–2010, same as in Figure 1(a)), closest gridpoint to the station (green curve, 20CRv2, 1872–2010), and instrumental time series of minimum temperature (T_n', blue curve, 1957–2010), maximum temperature (T_x', red curve, 1957–2010), and mean temperature (T_m', calculated as the average of T_n' and T_x', black curve, 1957–2010). Stations correspond to (top panel) Comodoro Rivadavia and (Bottom panel) Río Gallegos.

Figure S3. Changes in probability of rain exceeding 1 and 10 mm (black and white bars, respectively) during the 21-day sequence of days centred on day 0 for (a) Cataract Dam Station (Southeastern Australia) and (b) Hororata Station (South Island of New Zealand); see Table S1. The reference period is 1961–1990. Continuous blue and red curves depict the mean values obtained for events above 1 and 10 mm, respectively, through a Monte Carlo approach of 1000 random realizations; dashed curves represent the 25 and 75% percentiles of the corresponding distributions.

Table S1. November–March (NDJFM) precipitation statistics for two stations in Oceania.

References

Abram NJ, Mulvaney R, Vimeux F, Phipps SJ, Turner J, England MH. 2014. Evolution of the Southern Annular Mode during the past millennium. *Nat. Clim. Change* **4**: 564–569, doi: 10.1038/nclimate2235.

Alvarez M, Vera CS, Kiladis GN, Liebmann B. 2015. Influence of the Madden Julian Oscillation on precipitation and surface air temperature in South America. *Clim. Dyn.* 1–18, doi: 10.1007/s00382-015-2581-6.

Berbery EH, Nogués-Paegle J. 1993. Intraseasonal interactions between the tropics and extratropics in the Southern Hemisphere. *J. Atmos. Sci.* **50**: 1950–1965, doi: 10.1175/1520-0469(1993)050<1950:IIBTTA>2.0.CO;2.

Berman AL, Silvestri G, Compagnucci R. 2012. Eastern Patagonia seasonal precipitation: influence of Southern Hemisphere circulation and links with subtropical South American precipitation. *J. Clim.* **25**: 6781–6795, doi: 10.1175/JCLI-D-11-00514.1.

Berman A, Silvestri G, Compagnucci R. 2013. On the variability of seasonal temperature in southern South America. *Clim. Dyn.* **40**: 1863–1878, doi: 10.1007/s00382-012-1596-5.

Bromwich DH, Fogt RL, Hodges KI, Walsh JE. 2007. A tropospheric assessment of the ERA-40, NCEP, and JRA-25 global reanalyses in the polar regions. *J. Geophys. Res. Atmos.* **112**: D10111, doi: 10.1029/2006JD007859.

Brönnimann S, Compo GP, Spadin R, Allan R, Adam W. 2011. Early ship-based upper-air data and comparison with the Twentieth Century Reanalysis. *Clim. Past* **7**: 265–276, doi: 10.5194/cp-7-265-2011.

Brönnimann S, Grant AN, Compo GP, Ewen T, Griesser T, Fischer AM, Schraner M, Stickler A. 2012. A multi-data set comparison of the vertical structure of temperature variability and change over the Arctic during the past 100 years. *Arctic* **39**: 1577–1598.

Carrasco J, Casassa G, Rivera A. 2002. Meteorological and climatological aspects of the Southern Patagonia Icefield. In *The Patagonian Icefields SE – 4*, Casassa G, Sepúlveda F, Sinclair R (eds). Springer US, New York, USA, 29–41, doi: 10.1007/978-1-4615-0645-4_4.

Carvalho LMV, Jones C, Liebmann B. 2002. Extreme precipitation events in southeastern South America and large-scale convective patterns in the South Atlantic Convergence Zone. *J. Clim.* **15**: 2377–2394, doi: 10.1175/1520-0442(2002)015<2377:EPEISS>2.0.CO;2.

Cazes-Boezio G, Robertson AW, Mechoso CR. 2003. Seasonal dependence of ENSO teleconnections over South America and relationships with precipitation in Uruguay. *J. Clim.* **16**: 1159–1176, doi: 10.1175/1520-0442(2003)16<1159:SDOETO>2.0.CO;2.

Cerne SB, Vera CS. 2011. Influence of the intraseasonal variability on heat waves in subtropical South America. *Clim. Dyn.* **36**: 2265–2277, doi: 10.1007/s00382-010-0812-4.

Compagnucci RH, Agosta EA, Vargas WM. 2002. Climatic change and quasi-oscillations in central-west Argentina summer precipitation: main features and coherent behaviour with southern African region. *Clim. Dyn.* **18**: 421–435, doi: 10.1007/s003820100183.

Compo GP, Whitaker JS, Sardeshmukh PD, Matsui N, Allan RJ, Yin X, Gleason BE, Vose RS, Rutledge G, Bessemoulin P, Brönnimann S, Brunet M, Crouthamel RI, Grant AN, Groisman PY, Jones PD, Kruk M, Kruger AC, Marshall GJ, Maugeri M, Mok HY, Nordli Ø, Ross TF, Trigo RM, Wang XL, Woodruff SD, Worley SJ. 2011. The Twentieth Century Reanalysis Project. *Q. J. R. Meteorol. Soc.* **137**: 1–28, doi: 10.1002/qj.776.

Del Valle HF, Elissalde NO, Gagliardini DA, Milovich J. 1998. Status of desertification in the Patagonian region: assessment and mapping from satellite imagery. *Arid Soil Res. Rehabil.* **12**: 95–121, doi: 10.1080/15324989809381502. http://www.tandfonline.com/doi/abs/10.1080/15324989809381502.

Garreaud R. 2000. Cold air incursions over subtropical South America: mean structure and dynamics. *Mon. Weather Rev.* **128**: 2544–2559, doi: 10.1175/1520-0493(2000)128<2544:CAIOSS>2.0.CO;2.

Garreaud RD, Vuille M, Compagnucci R, Marengo J. 2009. Present-day South American climate. *Palaeogeogr. Palaeoclimatol. Palaeoecol.* **281**: 180–195, doi: 10.1016/j.palaeo.2007.10.032. http://www.sciencedirect.com/science/article/pii/S0031018208005002.

Garreaud R, Lopez P, Minvielle M, Rojas M. 2012. Large-scale control on the Patagonian climate. *J. Clim.* **26**: 215–230, doi: 10.1175/JCLI-D-12-00001.1.

Gillett NP, Kell TD, Jones PD. 2006. Regional climate impacts of the Southern Annular Mode. *Geophys. Res. Lett.* **33**: L23704, doi: 10.1029/2006GL027721.

Gonzalez PM, Vera C. 2014. Summer precipitation variability over South America on long and short intraseasonal timescales. *Clim. Dyn*. **43**: 1993–2007, doi: 10.1007/s00382-013-2023-2.

Hertel D, Therburg A, Villalba R. 2008. Above- and below-ground response by Nothofagus pumilio to climatic conditions at the transition from the steppe–forest boundary to the alpine treeline in southern Patagonia, Argentina. *Plant Ecol. Divers.* **1**: 21–33, doi: 10.1080/17550870802257026.

Hoskins BJ, Simmons AJ, Andrews DG. 1977. Energy dispersion in a barotropic atmosphere. *Q. J. R. Meteorol. Soc*. **103**: 553–567, doi: 10.1002/qj.49710343802.

Jacques-Coper M, Brönnimann S. 2014. Summer temperature in the eastern part of southern South America: its variability in the twentieth century and a teleconnection with Oceania. *Clim. Dyn.* **43**: 2111–2130, doi: 10.1007/s00382-013-2038-8.

Jacques-Coper M, Garreaud RD. 2014. Characterization of the 1970s climate shift in South America. *Int. J. Climatol*. **43**: 2111–2130, doi: 10.1002/joc.4120.

Jacques-Coper M, Brönnimann S, Martius O, Vera CS, Cerne SB. 2015. Evidence for a modulation of the intraseasonal summer temperature in Eastern Patagonia by the Madden–Julian Oscillation. *J. Geophys. Res. Atmos.* doi: 10.1002/2014JD022924.

Jin F, Hoskins BJ. 1995. The direct response to tropical heating in a baroclinic atmosphere. *J. Atmos. Sci.* **52**: 307–319, doi: 10.1175/1520-0469(1995)052<0307:TDRTTH>2.0.CO;2.

Jones JM, Fogt RL, Widmann M, Marshall GJ, Jones PD, Visbeck M. 2009. Historical SAM variability. Part I: century-length seasonal reconstructions*. *J. Clim.* **22**: 5319–5345, doi: 10.1175/2009JCLI2785.1.

Kalnay E, Kanamitsu M, Kistler R, Collins W, Deaven D, Gandin L, Iredell M, Saha S, White G, Woollen J, Zhu Y, Leetmaa A, Reynolds R, Chelliah M, Ebisuzaki W, Higgins W, Janowiak J, Mo KC, Ropelewski C, Wang J, Jenne R, Joseph D. 1996. The NCEP/NCAR 40-year reanalysis project. *Bull. Am. Meteorol. Soc.* **77**: 437–471, doi: 10.1175/1520-0477(1996)077<0437:TNYRP>2.0.CO;2.

Lara A, Villalba R, Wolodarsky-Franke A, Aravena JC, Luckman BH, Cuq E. 2005. Spatial and temporal variation in Nothofagus pumilio growth at tree line along its latitudinal range (35°40′–55° S) in the Chilean Andes. *J. Biogeogr.* **32**: 879–893, doi: 10.1111/j.1365-2699.2005.01191.x.

Lee S, Held IM. 1993. Baroclinic wave packets in models and observations. *J. Atmos. Sci.* **50**: 1413–1428, doi: 10.1175/1520-0469(1993)050<1413:BWPIMA>2.0.CO;2.

Liebmann B, Kiladis GN, Marengo J, Ambrizzi T, Glick JD. 1999. Submonthly convective variability over South America and the South Atlantic Convergence Zone. *J. Clim.* **12**: 1877–1891, doi: 10.1175/1520-0442(1999)012<1877:SCVOSA>2.0.CO;2.

Lima K, Satyamurty P, Fernández J. 2010. Large-scale atmospheric conditions associated with heavy rainfall episodes in Southeast Brazil. *Theor. Appl. Climatol.* **101**: 121–135, doi: 10.1007/s00704-009-0207-9.

Madden RA, Julian PR. 1971. Detection of a 40–50 day oscillation in the zonal wind in the tropical Pacific. *J. Atmos. Sci.* **28**: 702–708, doi: 10.1175/1520-0469(1971)028<0702:DOADOI>2.0.CO;2.

Marshall GJ. 2003. Trends in the Southern Annular Mode from observations and reanalyses. *J. Clim.* **16**: 4134–4143, doi: 10.1175/1520-0442(2003)016<4134:TITSAM>2.0.CO;2.

Mazzonia E, Vazquez M. 2009. Desertification in Patagonia. In *Natural Hazards and Human-Exacerbated Disasters in Latin America*. Developments in Earth Surface Processes, Vol. 13. Elsevier, 351–377. http://www.sciencedirect.com/science/article/pii/S0928202508100177.

Mo KC, Higgins RW. 1998. The Pacific–South American modes and tropical convection during the Southern Hemisphere winter. *Mon. Weather Rev.* **126**: 1581–1596, doi: 10.1175/1520-0493(1998)126<1581:TPSAMA>2.0.CO;2.

Müller GV, Berri GJ. 2007. Atmospheric Circulation associated with persistent generalized frosts in central-southern South America. *Mon. Weather Rev.* **135**: 1268–1289, doi: 10.1175/MWR3344.1.

Orlanski I, Chang EKM. 1993. Ageostrophic geopotential fluxes in downstream and upstream development of baroclinic waves. *J. Atmos. Sci.* **50**: 212–225, doi: 10.1175/1520-0469(1993)050<0212:AGFIDA>2.0.CO;2.

Paruelo JM, Beltran A, Jobbagy E, Sala OE, Golluscio RA. 1998. The climate of Patagonia: general patterns and controls on biotic. *Ecol. Aust.* **8**: 85–101.

Prohaska F. 1976. In *The Climate of Argentina, Paraguay, and Uruguay*, Vol. 12, Schwerdtfeger W (ed). Elsevier: Amsterdam, The Netherlands.

Rakich CS, Holbrook NJ, Timbal B. 2008. A pressure gradient metric capturing planetary-scale influences on eastern Australian rainfall. *Geophys. Res. Lett.* **35**: L08713, doi: 10.1029/2007GL032970.

Rasmussen LA, Conway H, Raymond CF. 2007. Influence of upper air conditions on the Patagonia icefields. *Glob. Planet. Change* **59**: 203–216, doi: 10.1016/j.gloplacha.2006.11.025. http://www.sciencedirect.com/science/article/pii/S0921818106002906.

Rignot E, Rivera A, Casassa G. 2003. Contribution of the Patagonia Icefields of South America to sea level rise. *Science* **302**: 434–437, doi: 10.1126/science.1087393. http://www.sciencemag.org/content/302/5644/434.abstract.

Robertson AW, Mechoso CR. 2003. Circulation regimes and low-frequency oscillations in the South Pacific sector. *Mon. Weather Rev.* **131**: 1566–1576, doi: 10.1175//2548.1.

Solman SA, Orlanski I. 2013. Poleward shift and change of frontal activity in the Southern Hemisphere over the last 40 years. *J. Atmos. Sci.* **71**: 539–552, doi: 10.1175/JAS-D-13-0105.1.

Sprenger M, Martius O, Arnold J. 2013. Cold surge episodes over southeastern Brazil – a potential vorticity perspective. *Int. J. Climatol.* **33**: 2758–2767, doi: 10.1002/joc.3618.

Thompson DWJ, Solomon S. 2002. Interpretation of recent Southern Hemisphere climate change. *Science* **296**: 895–899, doi: 10.1126/science.1069270. http://www.sciencemag.org/content/296/5569/895.abstract.

Ummenhofer CC, England MH. 2007. Interannual extremes in New Zealand precipitation linked to modes of Southern Hemisphere climate variability. *J. Clim.* **20**: 5418–5440, doi: 10.1175/2007JCLI1430.1. http://journals.ametsoc.org/doi/abs/10.1175/2007JCLI1430.1 (Accessed August 14, 2013).

Uppala SM, Kållberg PW, Simmons AJ, Andrae U, Bechtold VDC, Fiorino M, Gibson JK, Haseler J, Hernandez A, Kelly GA, Li X, Onogi K, Saarinen S, Sokka N, Allan RP, Andersson E, Arpe K, Balmaseda MA, Beljaars ACM, Van De Berg L, Bidlot J, Bormann N, Caires S, Chevallier F, Dethof A, Dragosavac M, Fisher M, Fuentes M, Hagemann S, Hólm E, Hoskins BJ, Isaksen L, Janssen PAEM, Jenne R, Mcnally AP, Mahfouf J-F, Morcrette J-J, Rayner NA, Saunders RW, Simon P, Sterl A, Trenberth KE, Untch A, Vasiljevic D, Viterbo P, Woollen J. 2005. The ERA-40 re-analysis. *Q. J. R. Meteorol. Soc.* **131**: 2961–3012, doi: 10.1256/qj.04.176.

Wang G, Cai W. 2013. Climate-change impact on the 20th-century relationship between the Southern Annular Mode and global mean temperature. *Sci. Rep.* **3**: 1–6, doi: 10.1038/srep02039.

Zhang C. 2005. Madden-Julian Oscillation. *Rev. Geophys.* **43**: RG2003, doi: 10.1029/2004RG000158.

Zhang C. 2013. Madden–Julian Oscillation: bridging weather and climate. *Bull. Am. Meteorol. Soc.* **94**: 1849–1870, doi: 10.1175/BAMS-D-12-00026.1.

Zhang Q, Körnich H, Holmgren K. 2012. How well do reanalyses represent the southern African precipitation? *Clim. Dyn.* **40**: 951–962, doi: 10.1007/s00382-012-1423-z. http://link.springer.com/10.1007/s00382-012-1423-z (Accessed April 3, 2013).

